Check for updates

ADVANCED HEALTHCARE MATERIALS
www.advhealthmat.de

Immune Cell-Based Microrobots for Remote Magnetic Actuation, Antitumor Activity, and Medical Imaging

*Nihal Olcay Dogan, Eylül Suadiye, Paul Wrede, Jelena Lazovic, Cem Balda Dayan, Ren Hao Soon, Amirreza Aghakhani, Gunther Richter, and Metin Sitti**

Translating medical microrobots into clinics requires tracking, localization, and performing assigned medical tasks at target locations, which can only happen when appropriate design, actuation mechanisms, and medical imaging systems are integrated into a single microrobot. Despite this, these parameters are not fully considered when designing macrophage-based microrobots. This study presents living macrophage-based microrobots that combine macrophages with magnetic Janus particles coated with FePt nanofilm for magnetic steering and medical imaging and bacterial lipopolysaccharides for stimulating macrophages in a tumor-killing state. The macrophage-based microrobots combine wireless magnetic actuation, tracking with medical imaging techniques, and antitumor abilities. These microrobots are imaged under magnetic resonance imaging and optoacoustic imaging in soft-tissue-mimicking phantoms and ex vivo conditions. Magnetic actuation and real-time imaging of microrobots are demonstrated under static and physiologically relevant flow conditions using optoacoustic imaging. Further, macrophage-based microrobots are magnetically steered toward urinary bladder tumor spheroids and imaged with a handheld optoacoustic device, where the microrobots significantly reduce the viability of tumor spheroids. The proposed approach demonstrates the proof-of-concept feasibility of integrating macrophage-based microrobots into clinic imaging modalities for cancer targeting and intervention, and can also be implemented for various other medical applications.

1. Introduction

Wireless medical microrobots have significant potential for minimally invasive targeted therapeutic interventions within the human body.[1–4] To date, various mobile microrobotic platforms have been proposed utilizing materials incompatible with physiological environments. The immune system, however, recognizes any physiologically incompatible material entering the body as a foreign invader and attacks to eliminate it, thus preventing such mobile microrobots from accomplishing their intended tasks.[5] This issue can be resolved by implementing patient-derived biomaterials, particularly immune system components, into medical microrobots.[6] The construction of medical microrobots with immune cells ensures their safety upon infusion into the patient, allowing them to remain in the body for an extended period.[7] More significantly, immune cells are living entities, acting like "living drugs."[8] Hence, immune cell-based therapies constantly produce treatment molecules and elicit desired effects longer than natural or synthetic drug molecules.[9–13] These

N. O. Dogan, P. Wrede, J. Lazovic, C. B. Dayan, R. H. Soon, A. Aghakhani, M. Sitti
Physical Intelligence Department
Max Planck Institute for Intelligent Systems
70569 Stuttgart, Germany
E-mail: sitti@is.mpg.de

The ORCID identification number(s) for the author(s) of this article can be found under https://doi.org/10.1002/adhm.202400711

© 2024 The Author(s). Advanced Healthcare Materials published by Wiley-VCH GmbH. This is an open access article under the terms of the Creative Commons Attribution License, which permits use, distribution and reproduction in any medium, provided the original work is properly cited.

DOI: 10.1002/adhm.202400711

N. O. Dogan, P. Wrede, R. H. Soon, M. Sitti
Institute for Biomedical Engineering
ETH Zurich
Zurich 8092, Switzerland

E. Suadiye, G. Richter
Materials Central Scientific Facility
Max Planck Institute for Intelligent Systems
70569 Stuttgart, Germany

A. Aghakhani
Institute of Biomaterials and Biomolecular Systems
University of Stuttgart
70569 Stuttgart, Germany

M. Sitti
School of Medicine and College of Engineering
Koç University
Istanbul 34450, Turkey

benefits enable immune cell therapies to treat diseases with enhanced performance.[14]

Macrophages, an immune system component, have essential physiological features that can be helpful for medical microrobots.[6,15–19] Almost all body tissues contain macrophages, and they are one of the first cells to reach diseased sites.[20,21] Moreover, macrophages engulf and digest invading materials (i.e., bacteria, viruses, damaged cells, and foreign particles) with an inherent "phagocytosis" process, making them ideal carriers for therapeutics and imaging agents for cell tracking.[19,22] Due to their ability to detect and migrate to tumors by penetrating biological barriers, macrophages have been promising therapeutic prospects in cancer immunotherapy.[23] Inside the tumor microenvironment, macrophages either inhibit (M1 phenotype) or promote (M2 phenotype) tumor growth based on physiological factors.[24] M1 phenotype macrophages can distinguish tumor cells from healthy ones and ultimately eliminate tumor cells using various mechanisms. These mechanisms include the secretion of harmful products, such as reactive oxygen species (ROS) and nitric oxide (NO), recognition and binding to antibody-coated cancer cells, and recruitment of other host immune cells capable of destroying cancer cells.[25,26] Therefore, macrophage-based therapies in cancer treatment focus on maintaining M1 phenotype macrophages with antitumorigenic properties.[27] Mainly, exposure of macrophages to bacterial cell wall lipopolysaccharides (LPS) initiates a signal cascade by interacting with toll-like receptor 4 (TLR4) of the cells, resulting in macrophage activation into M1 phenotype and enhanced production and release of tumor-fighting molecules.[28]

Despite their impressive therapeutic benefits, macrophages are still constrained by certain limitations. An effective macrophage therapy relies on the efficient delivery and retention of cells in target tissues.[29] However, distinct challenges remain in actuating and localizing a sufficient number of macrophages to the desired site. The solution to this problem relies on finding the proper actuation mechanism and real-time tracking signal through a suitable medical imaging system.[30,31] Among different actuation methods, magnetic actuation can enable the transportation of a swarm of macrophages remotely and precisely in a noninvasive manner, thereby improving treatment efficacy.[6,32–35] Meanwhile, many therapeutic cells (e.g., macrophages, neutrophils, stem cells, and T cells) are transparent and must be labeled with contrast agents for long-term cell tracking with medical imaging techniques.[32,36] Since no medical imaging method can fully track cell-sized microrobots within the body at all angles with a reasonable spatiotemporal resolution, using multimodal contrast agents detectable by several medical imaging techniques becomes advantageous.[37,38] Therefore, labeling macrophages with multimodal contrast agents could enable their detection under multiple imaging modalities, providing more comprehensive diagnostic information about macrophage fate and their therapeutic interventions within the body.

Here, we report macrophage-based microrobots, "immunobots",[6] composed of living macrophages that internalize magnetic Janus particles using their intrinsic phagocytosis capability. The magnetic Janus particles are made from silica particles half-coated with FePt magnetic nanofilm and half-coated with bacterial LPS. Here, the FePt magnetic nanofilm has two main functionalities on macrophage-based microrobots: i) FePt is a biocompatible and strong magnetic material that enables remote and precise magnetic actuation and steering of a swarm of macrophage-based microrobots via external magnetic fields to a target location; ii) FePt has the potential to serve as a multimodal contrast agent detectable under magnetic resonance imaging (MRI) and optoacoustic (OA) imaging, also termed as photoacoustic imaging or optoacoustic tomography. Furthermore, bacterial LPS coating on magnetic Janus particles stimulates macrophages into an anticancer state (M1) to make the engineered macrophage-based microrobots capable of fighting cancer.

Among different imaging techniques, we focused on well-established safe (nonradiation) medical imaging techniques: MRI and OA imaging. Based on the multimodal contrast effect of FePt, the developed macrophage-based microrobots were detected using MRI and OA imaging in soft-tissue-mimicking phantoms and ex vivo conditions. Moreover, we tracked macrophage-based microrobots in real time using OA imaging as they moved toward the target location in static and physiologically relevant flow conditions. Furthermore, the M1 characterization of macrophage-based microrobots was performed by measuring the secreted amounts of M1 cytokines, including interleukin-12 (IL-12), tumor necrosis factor-alpha (TNF-α), and interleukin-6 (IL-6). The antitumor abilities of macrophage-based microrobots were investigated through their co-culture with monolayer bladder cancer cells and 3D tumor spheroids. The macrophage-based microrobots were magnetically guided toward urinary bladder 3D tumor spheroids while imaging with the OA device, where the microrobots significantly decreased the viability of 3D tumor spheroids. Here, wireless magnetic actuation, tracking with well-established medical imaging techniques, and performing 3D tumor spheroid treatment in vitro or ex vivo have been integrated into a single biohybrid macrophage-based microrobot design. The macrophage-based microrobots described in this paper, thus, have a strong clinical potential for future cancer treatment applications while eliminating side effects and immune responses.

2. Results and Discussions

2.1. Concept of Macrophage-Based Microrobots

We developed macrophage-based microrobots from living macrophages that internalized magnetic Janus particles using their inherent phagocytosis capability (**Figure 1A**). First, magnetic Janus particles were prepared from 500 nm diameter silica beads, half-coated with FePt magnetic nanofilm and half-coated with bacterial LPS. Here, we selected FePt because of its biocompatibility,[6] strong magnetic properties,[37] and ability to be used as a contrast agent for cell labeling and detection under different imaging techniques,[39,40] all of which are essential features for medical microrobots. The FePt coating (60 nm thickness) on silica particles was confirmed through scanning electron microscopy (SEM) and transmission electron microscopy (TEM) (Figure S1, Supporting Information). In addition, we investigated the magnetic properties of FePt-coated silica particles using a vibrating sample magnetometer (VSM), where the results

© 2024 The Author(s). Advanced Healthcare Materials published by Wiley-VCH GmbH

21922659, 2024, 23, Downloaded from https://onlinelibrary.wiley.com/doi/10.1002/adhm.202400711 by Koc University, Wiley Online Library on [27/12/2024]. See the Terms and Conditions (https://onlinelibrary.wiley.com/terms-and-conditions) on Wiley Online Library for rules of use; OA articles are governed by the applicable Creative Commons License

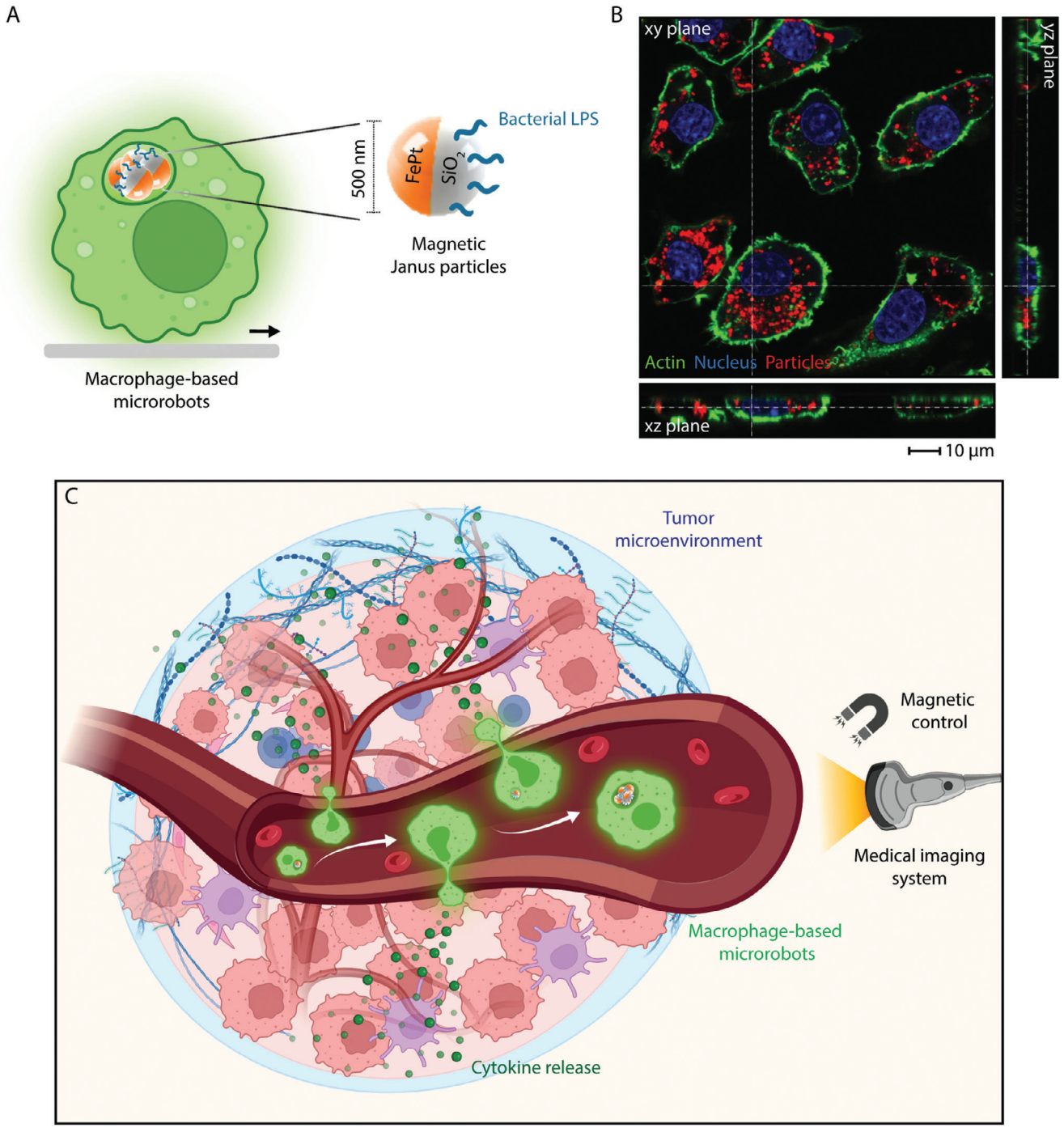


Figure 1. Medical imaging-guided magnetic actuation of macrophage-based microrobots for targeted cancer treatment. A) Macrophage-based microrobots were developed from living macrophages that internalized magnetic Janus particles, consisting of 500 nm diameter silica particles half-coated with FePt magnetic nanofilm and half-coated with bacterial LPS. B) Confocal images of macrophage-based microrobots indicating accumulation of magnetic Janus particles at the inner border of macrophages. C) A conceptual schematic depicts a swarm of macrophage-based microrobots that can be magnetically actuated and accumulated at a target tumor location by receiving feedback from medical imaging systems, resulting in enhanced anticancer abilities with minimal toxicity to the body.

© 2024 The Author(s). Advanced Healthcare Materials published by Wiley-VCH GmbH

21922659, 2024, 23, Downloaded from https://onlinelibrary.wiley.com/doi/10.1002/adhm.202400711 by Koc University, Wiley Online Library on [27/12/2024]. See the Terms and Conditions (https://onlinelibrary.wiley.com/terms-and-conditions) on Wiley Online Library for rules of use; OA articles are governed by the applicable Creative Commons License

indicated a coercivity of 785 mT (Figure S2, Supporting Information).

After confirming the FePt coating, our next step was to conjugate bacterial LPS to the uncoated side of the silica particles. The bacterial LPS enabled us to control the activation states of macrophages toward the anticancer (M1) state.[6] Several chemical reactions were performed to conjugate the bacterial LPS to FePt-coated silica particles, including biotin and streptavidin interaction, which has a high affinity and strong binding properties (Figure S3A, Supporting Information). We confirmed the conjugation of fluorescein isothiocyanate (FITC)-tagged streptavidin onto biotinylated ends of FePt-coated silica particles with fluorescence microscopy (Figure S3B, Supporting Information). The streptavidin-conjugated particles were further modified with biotinylated bacterial LPS, where the biotinylated end of the bacterial LPS exhibited a very high affinity for streptavidin.[41] The resultant silica beads modified with FePt magnetic nanofilm and bacterial LPS were called magnetic Janus particles.

As a next step, living macrophages were incubated with magnetic Janus particles overnight to prepare macrophage-based microrobots. Magnetic Janus particles were phagocytosed by macrophages, resulting in the development of magnetically controllable, antitumorigenic (M1 phenotype) macrophage-based microrobots (Figure 1A). To verify that macrophages fully internalized the magnetic Janus particles, we fluorescently stained the nuclei and actin filament compartments of cells. The confocal images confirmed that fluorescently labeled magnetic Janus particles accumulated at the inner borders of macrophages after overnight incubation (Figure 1B). Due to the advantages of the FePt magnetic nanofilm layer of magnetic Janus particles, the macrophage-based microrobots developed here could be magnetically controlled, imaged under different medical imaging techniques, and due to the bacterial LPS, the macrophage-based microrobots were capable of fighting cancer as a result of their antitumorigenic (M1) activation states (Figure 1C). All the characterizations of macrophage-based microrobots (e.g., encapsulation efficiency of cells, biocompatibility assessment, magnetic properties of bare macrophages and macrophage-based microrobots, magnetic actuation and steering, and preparation of microrobots from primarily isolated cells) are shown in Figures S4–S12 (Supporting Information).

Macrophages have recently become promising candidates in treating solid tumors since these cells can infiltrate tumors, unlike lymphocytes.[6,42] It has been demonstrated that macrophages can kill tumor cells by exerting phagocytic and cytotoxic functions, secreting proinflammatory M1 cytokines, presenting tumor-specific antigens for adaptive antitumor immunity induction, and facilitating innate immune cells recruitment into tumor microenvironments.[43–45] Local or systemic injections of M1-polarized macrophages have also been shown to have in vivo antitumor effects on several murine tumor models, such as ovarian, breast, and lung.[11,43] Our macrophage-based biohybrid microrobots have considerable potential to improve the tumor-targeting and antitumor capabilities of M1 macrophages by actuating and accumulating a swarm of macrophages at target locations upon magnetic control, resulting in enhanced anticancer efficacy with minimized toxicity to the body.

2.2. Medical Imaging of Macrophage-Based Microrobots

Macrophage-based microrobots can only successfully perform their assigned tasks once they reach the target area, which is only possible by getting continuous feedback from medical imaging modalities.[46] Thus far, several imaging modalities have been proposed.[31] We used MRI and OA imaging from different techniques for real-time imaging of macrophage-based microrobots, as these modalities are safe, noninvasive medical imaging techniques.[37,47–50] MRI is the most common imaging modality routinely used in clinical diagnostics, with excellent soft tissue contrast and high-resolution capabilities. Even though MRI is considered a low signal-to-noise imaging modality, using various contrast agents can aid in signal-to-noise and contrast-to-noise enhancements.[47,48] In this work, FePt particles act as T_2^*-contrast agents, causing local signal loss due to their magnetic field. For T_2^*-contrast agents, it is typical that the region of signal loss can be ≈100 times larger than the particles themselves, therefore greatly helping the visualization of microrobots.[37,51] An alternative imaging method is OA imaging, where a tissue absorbs light pulses, expands, and releases ultrasonic waves detected by an acoustic detector.[52] OA is a fast imaging technique enabling real-time 3D monitoring of dynamic biological processes.[52,53] Furthermore, it provides micrometer-scale high-resolution and molecular imaging capabilities; however, it has lower resolution and sensitivity than MRI.[54,55] Both imaging techniques have their advantages and disadvantages in this respect.

Macrophages are transparent and must be labeled with contrast agents to be detectable in medical imaging tools.[56] Contrast agents produce sufficient positive or negative signals to distinguish therapeutic cells from their surrounding tissue and make them noticeable under imaging systems.[32,57,58] Thus, macrophages labeled with contrast agents can be traceable inside the body with medical imaging techniques. Here, as FePt magnetic nanofilm on Janus particles is a multimodal contrast agent, we were capable of tracking macrophages that engulfed magnetic Janus particles using different imaging techniques, MRI and OA imaging. The FePt labeling approach used in this paper can provide long-term macrophage tagging without compromising their function and eliminate the requirement to inject harmful radiolabeled contrast agents or genetic modifications into the cells.

We performed the medical imaging of macrophage-based microrobots inside soft-tissue-mimicking phantoms, as the human body primarily comprises soft tissues (**Figure 2A**).[59] We used agar as a soft-tissue-mimicking phantom since it is widely used in medical imaging due to its ability to mimic the mechanical properties of soft living tissues.[60–62] We embedded macrophage-based microrobots and macrophages in their bare forms in soft-tissue-mimicking phantoms at different concentrations (500 000, 250 000, 100 000, 50 000, 10 000, and 1000 cells in a 100 µL volume), as at least one million engineered cells are typically injected into mice in vivo in the literature.[17,18,63] In MRI scans, macrophage-based microrobots gave a negative contrast (signal loss) in the T_2^*-weighted image due to the high saturation magnetization of FePt. The increased concentration of macrophage-based microrobots showed more signal loss and darker areas on MRI scans, while bare macrophages displayed no contrast. Due to the high magnetization of magnetic Janus particles, we could visualize as little as 1000 macrophage-based

© 2024 The Author(s). Advanced Healthcare Materials published by Wiley-VCH GmbH

21922659, 2024, 23, Downloaded from https://onlinelibrary.wiley.com/doi/10.1002/adhm.202400711 by Koc University, Wiley Online Library on [27/12/2024]. See the Terms and Conditions (https://onlinelibrary.wiley.com/terms-and-conditions) on Wiley Online Library for rules of use; OA articles are governed by the applicable Creative Commons License

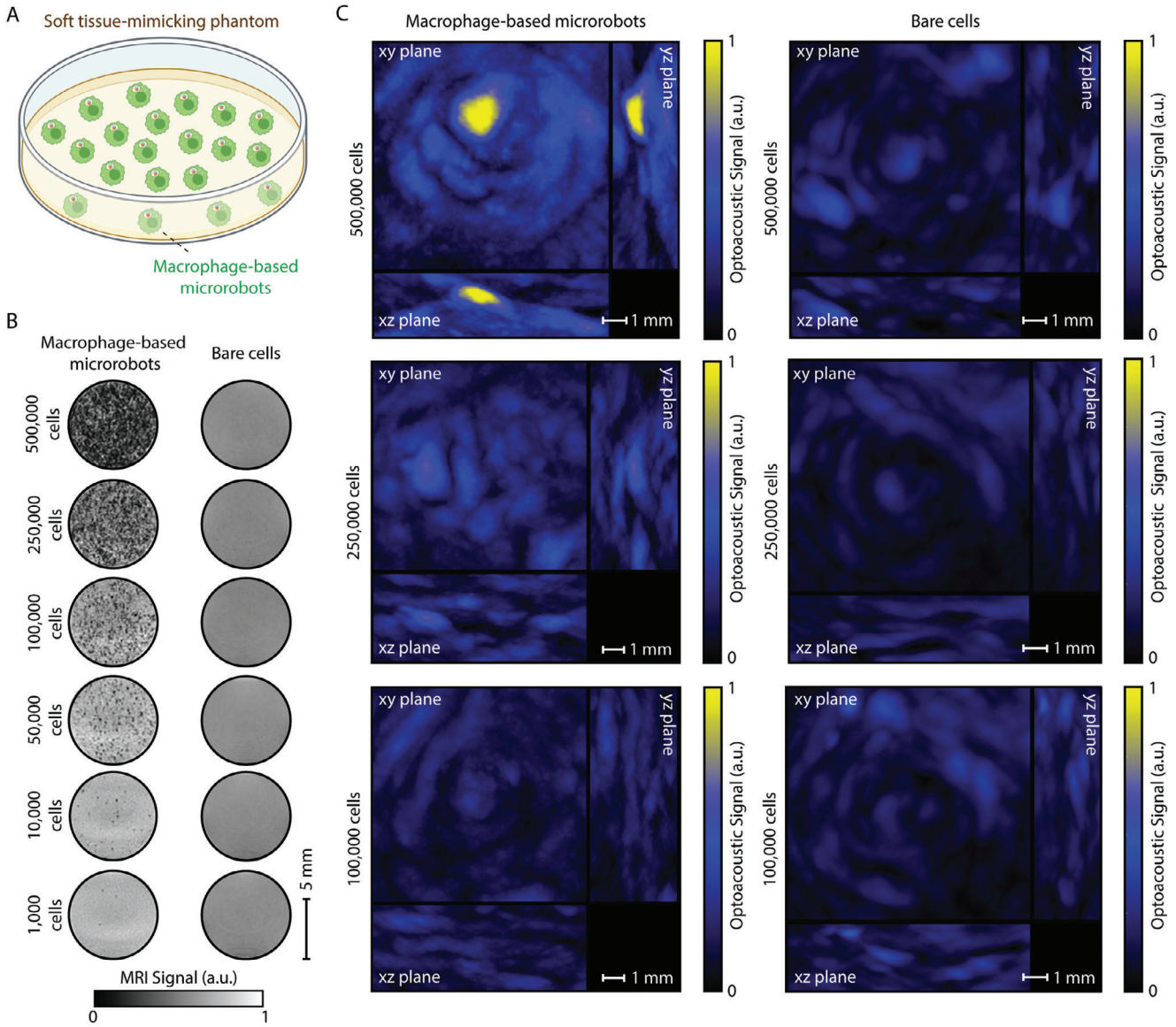


Figure 2. MRI and OA medical imaging results of macrophage-based microrobots in soft-tissue-mimicking phantoms. A) A conceptual schematic depicts macrophage-based microrobots embedded in soft-tissue-mimicking phantoms. B) Macrophage-based microrobots and bare macrophages immersed in soft-tissue-mimicking phantoms at various concentrations (500 000, 250 000, 100 000, 50 000, 10 000, and 1000 cells in a 100 µL volume) were analyzed using MRI. C) Macrophage-based microrobots and bare macrophages immersed in soft-tissue-mimicking phantoms at various concentrations (500 000, 250 000, and 100 000 cells in a 100 µL volume) were analyzed using OA imaging.

microrobots in soft-tissue-mimicking phantoms (Figure 2B; Figure S13, Supporting Information). In OA imaging, macrophage-based microrobots showed strong absorbances at 840 nm; therefore, all the images for both groups (i.e., bare macrophages and macrophage-based microrobots) were captured at that wavelength. The increasing concentrations of macrophage-based microrobots gave an increased signal through OA imaging. We could detect 250 000 macrophage-based microrobots in a soft-tissue-mimicking phantom with OA imaging (Figure 2C).

Our next step was to examine the imaging potential of macrophage-based microrobots within biological tissues by performing ex vivo experiments using fresh dead mice. For these experiments, we injected macrophage-based microrobots and bare macrophages into the right and left back muscles of the dead mouse and visualized them in MRI and OA imaging (**Figure** 3A). We injected macrophage-based microrobots and bare macrophages at different concentrations (250 000, 166 667, and 1667 cells in a 20 µL injection volume) into the dead mouse for MRI. The whole-body MRI scans of the dead animals were performed before and after the injections. T_2^*-weighted MRI analysis revealed that macrophage-based microrobots showed a local negative contrast at the injection site, whereas bare macrophages showed no contrast (Figure 3B). In MRI scans, ≈1667 macrophage-based microrobots were visible inside the animal tissue. In addition, macrophage-based

© 2024 The Author(s). Advanced Healthcare Materials published by Wiley-VCH GmbH

21922659, 2024, 23, Downloaded from https://onlinelibrary.wiley.com/doi/10.1002/adhm.202400711 by Koc University, Wiley Online Library on [27/12/2024]. See the Terms and Conditions (https://onlinelibrary.wiley.com/terms-and-conditions) on Wiley Online Library for rules of use; OA articles are governed by the applicable Creative Commons License

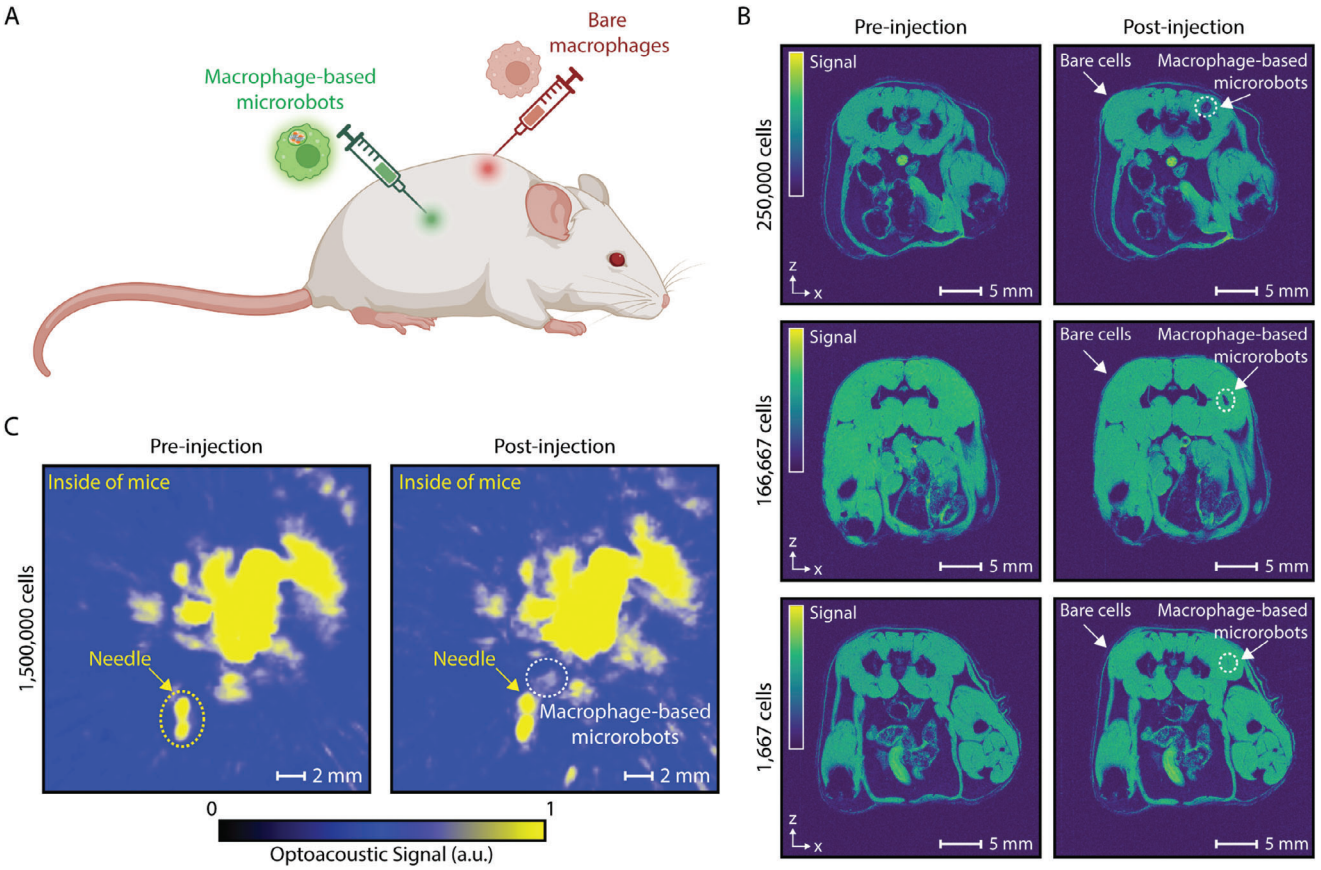


Figure 3. Ex vivo MRI and OA medical imaging results of macrophage-based microrobots. A) A schematic depicts bare macrophages and macrophage-based microrobots injected into a dead mouse for medical imaging. B) Ex vivo MRI of bare macrophages and macrophage-based microrobots at various concentrations (250 000, 166 667, and 1667 cells in a 20 µL injection volume) before and after the injection. C) Needle-guided ex vivo OA imaging of macrophage-based microrobots (1500 000 macrophage-based microrobots in a 50 µL injection volume).

microrobots were examined inside the porcine brain using MRI. The frontal porcine brain was injected with different concentrations of macrophage-based microrobots: 1250 cells μL^{-1} (50 000 macrophage-based microrobots in a 40 µL injection volume) and 2500 cells μL^{-1} (50 000 macrophage-based microrobots in a 20 µL injection volume). T_2^*-weighted MRI analysis has shown that macrophage-based microrobots were easily distinguished from the brain vasculature and caused a local negative contrast around the injection site (Figures S14 and S15, Supporting Information). Next, we analyzed ex vivo OA imaging of macrophage-based microrobots through a needle-guided injection with 1500 000 cells in a 50 µL injection volume into the dead animal (Figure 3C; Video S1, Supporting Information). Currently, medical imaging has some challenges due to imperfections in the body, significant differences in pathology, and high background noise levels.[64] Thus, medical image interpretation has recently benefited from advanced computer-aided analysis techniques based on background subtraction to interpret medical images better.[64] In this context, advanced image analysis with background subtraction technique can be applied to macrophage-based microrobots to improve OA imaging quality in future work.

To summarize, ex vivo imaging results of macrophage-based microrobots were similar to the soft-tissue-mimicking phantoms. The results indicated that due to the high saturation magnetization of magnetic Janus particles, the sensitivity of MRI to detect the low number of macrophage-based microrobots in both soft-tissue-mimicking phantoms and ex vivo was much better than OA imaging. Even though we obtained better sensitivity and higher-resolution images with MRI, it is unsuitable for real-time medical imaging due to longer scan duration. Conversely, OA imaging is less sensitive than MRI, where the contrast-to-noise ratio of OA imaging can be further improved by integrating additional contrast agents. More importantly, OA is a high-speed imaging technique that allows real-time image-guided navigation.

2.3. Optoacoustic Imaging-Guided Magnetic Actuation of Macrophage-Based Microrobots

From many different actuation mechanisms, magnetic manipulation can enable the remote and precise control of a single or swarm of magnetized objects in a noninvasive manner, which could result in increased effect, duration, and efficacy of macrophage-based therapies.[29] Therefore, we applied a magnetic particle labeling strategy to the macrophages, allowing us to remotely control a swarm of macrophages to a targeted location using external magnetic fields. Due to the long MRI scan time,

© 2024 The Author(s). Advanced Healthcare Materials published by Wiley-VCH GmbH

21922659, 2024, 23, Downloaded from https://onlinelibrary.wiley.com/doi/10.1002/adhm.202400711 by Koc University, Wiley Online Library on [27/12/2024]. See the Terms and Conditions (https://onlinelibrary.wiley.com/terms-and-conditions) on Wiley Online Library for rules of use; OA articles are governed by the applicable Creative Commons License

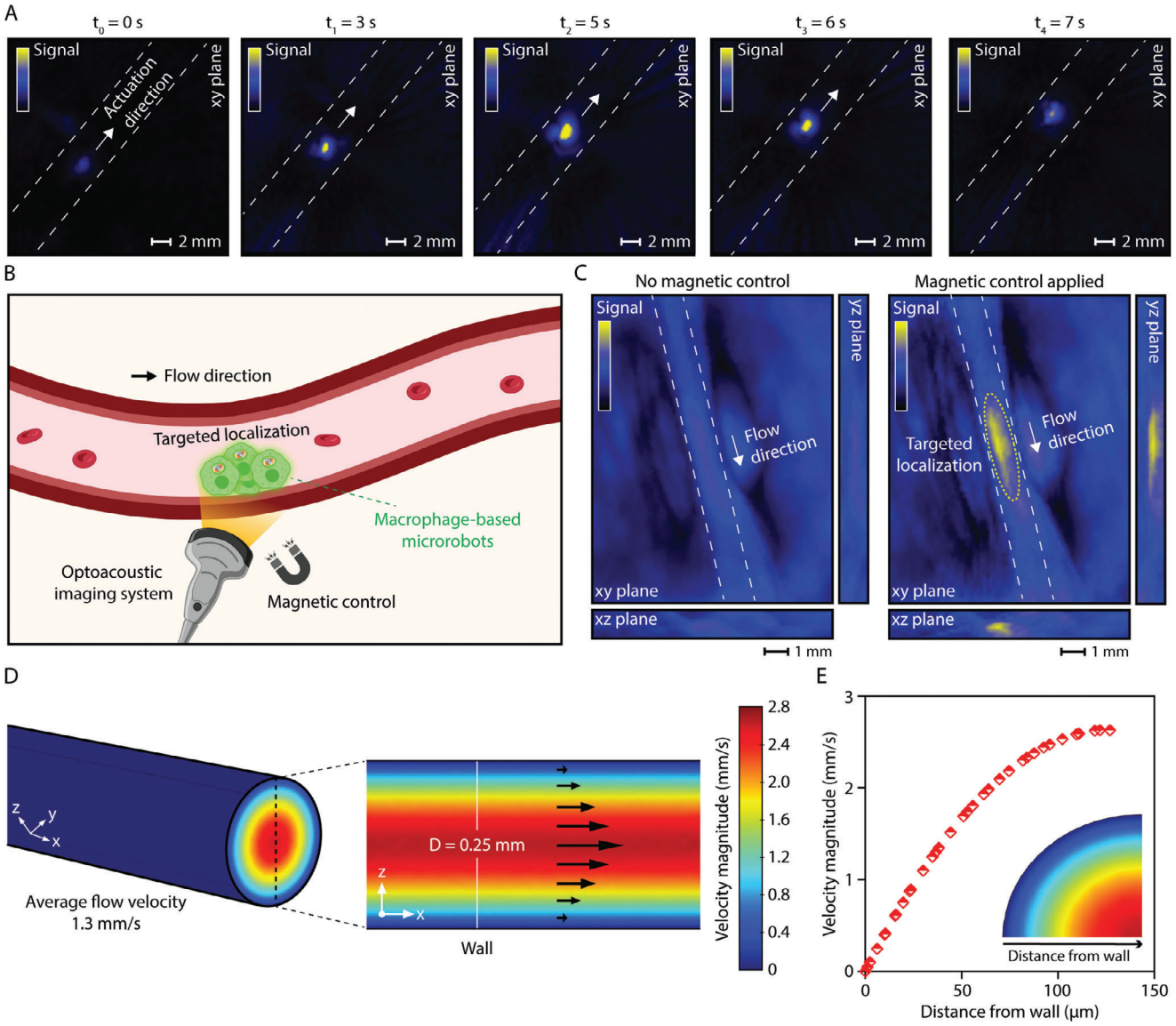


Figure 4. Real-time medical imaging and magnetic actuation of macrophage-based microrobots in static and flow conditions. A) The macrophage-based microrobots were magnetically steered at static conditions and imaged with OA imaging in real time. B) A schematic shows the targeted localization of macrophage-based microrobots by receiving feedback from the medical imaging system under flow conditions. C) The macrophage-based microrobots were localized in a target site using OA imaging under physiologically relevant flow conditions. D) FEM simulations analyze the flow through the tubing using an average flow velocity of 1.3 mm s^{-1} and a tubing size of 0.25 mm. E) The relation between the velocity magnitude and distance from the tubing wall.

navigation, real-time imaging, and tracking are difficult for dynamic biological organisms compared to OA imaging. Our group has also demonstrated the current upper limit of particle size for effective actuation to be around 500 μm for MRI.[48] Below this size, the magnetization of the particles is not sufficient for effective actuation using magnetic field gradients (as strong as 1 T m^{-1}). Therefore, actuation experiments of macrophage-based microrobots were conducted using OA imaging.

We investigated the active targeting of macrophage-based microrobots in static and flow conditions. First, the macrophage-based microrobots were injected into the tubing, and their position was controlled using an external magnetic field with gradient pulling in static conditions. By getting help from the fast imaging property of OA imaging, we visualized the position of macrophage-based microrobots in real time, with an average velocity of 1 mm s^{-1} (**Figure** 4A; Video S2, Supporting Information). We further investigated the active targeting of macrophage-based microrobots under physiologically relevant flow conditions (Figure 4B). We indicated OA-imaging-guided targeted localization of macrophage-based microrobots under an average flow rate of 1.3 mm s^{-1}, mimicking the flow rates of venules and capillaries (Figure 4C; Video S3, Supporting Information).[2] The macrophage-based microrobots were gathered in the target area using external magnetic fields and imaged

© 2024 The Author(s). Advanced Healthcare Materials published by Wiley-VCH GmbH

21922659, 2024, 23, Downloaded from https://onlinelibrary.wiley.com/doi/10.1002/adhm.202400711 by Koc University, Wiley Online Library on [27/12/2024]. See the Terms and Conditions (https://onlinelibrary.wiley.com/terms-and-conditions) on Wiley Online Library for rules of use; OA articles are governed by the applicable Creative Commons License

simultaneously using OA imaging. A magnetic field applied to a target location caused macrophage-based microrobots to cluster around that location, allowing for easy detection and visualization of macrophage-based microrobots over time. As a result of this experiment, macrophage-based microrobots can be actively controlled in physiologically relevant flow conditions to target tumor areas with a high degree of visualization and detection. In addition, we used finite element method (FEM) simulations by using the tubing dimensions and average flow velocity used in the experiments. The simulation results indicated the parabolic flow profile for the circular cross-sectional tubing, where the velocity magnitude increased as the distance from the tubing wall increased (Figure 4D,E). Combining magnetic control and targeted localization with real-time imaging in physiological flow conditions, we demonstrated the potential of macrophage-based microrobots for future in vivo applications.

2.4. Antitumor Activities of Macrophage-Based Microrobots

Bacterial LPS activates macrophages by interacting with TLR4 receptors of cells and altering their phenotypes into the antitumorigenic (M1) state.[28] A bacterial LPS coating on magnetic Janus particles thus enabled us to regulate macrophage activation into the M1 state. We characterized the activation states of macrophage-based microrobots by measuring the secreted amounts of IL-12, TNF-α, and IL-6 as M1 cytokines and IL-10 as M2 cytokine. The M1 cytokines play a crucial role in tumor suppression. IL-12 enhances the cytotoxicity of natural killer cells and cytotoxic T cells.[33] TNF-α induces endothelial cell apoptosis and allows chemotherapeutic agents to diffuse into the tumor microenvironment, thus disrupting tumor vasculature.[65] IL-6 regulates the trafficking of immune cells into tumors, therefore inhibiting cancer progression.[66] For M1 characterization experiments, the conditioned medium of macrophage-based microrobots and bare macrophages was harvested, and cytokine levels in the culture medium were compared in two groups. The results indicated that compared to bare macrophages, macrophage-based microrobots secreted higher amounts of M1 cytokines, while no significant changes were observed in the production of M2 cytokines (**Figure 5A**; Figure S16, Supporting Information).

Antitumorigenic M1 macrophages kill cancer cells by directly killing through the secretion of harmful products such as NO and ROS or indirectly killing by recruiting host immune cells to the tumor site.[67] In this study, we investigated the direct killing mechanisms of M1-activated macrophage-based microrobots using a transwell permeable system supported by 0.4 μm pores. We selected 0.4 μm pore size membranes suitable for co-culture applications, cytokine secretion, and drug transport studies.[68] The bare macrophages or macrophage-based microrobots were seeded in the upper compartment, whereas the urinary bladder cancer cells were seeded in the bottom compartment (Figure 5B). At 24 h of the co-culture experiment, the cellular viability of cancer cells was measured according to membrane integrity and metabolic activity measurements. Membrane integrity measurements were performed using a live/dead staining solution initially containing nonfluorescent molecules: calcein-AM and ethidium bromide-1. Calcein-AM passes through the cell membrane and is converted to a green fluorescent calcein (Ex/Em: 488/520 nm) in live cells upon hydrolysis of lipophilic groups. Conversely, ethidium bromide-1 is a highly positively charged molecule that can only pass through damaged cell membranes, bind to the DNA, and emit a red fluorescent signal (Ex/Em: 528/617 nm) in dead cells. The results of membrane integrity measurements demonstrated that co-culturing cancer cells with macrophage-based microrobots resulted in mostly dead cells, whereas co-culturing cancer cells with bare macrophages led to most cancer cells remaining alive (Figure 5B). Measuring membrane integrity provides information on cell viability but not cell proliferation. Therefore, we also evaluated the metabolic activities of cancer cells co-cultured with bare macrophages or macrophage-based microrobots. Since only viable cells can synthesize adenosine-5′-triphosphate (ATP), we measured the intracellular ATP as an indicator of cell viability. The metabolic activity results indicated that the viability of cancer cells reduced to 19% at 24 h when co-cultured with M1-activated macrophage-based microrobots (Figure 5C).

Second, we demonstrated the anticancer activity of macrophage-based microrobots on 3D tumor spheres developed from urinary bladder cancer cells in ultralow attachment plates (**Figure 6A**). The low adhesion of the cultureware prevented urinary bladder cells from adhering to the surface, encouraged cell-to-cell aggregation via naturally secreted extracellular matrices, and resulted in 3D tumor spheroids (Figure 6B). To demonstrate the OA-imaging-guided actuation of macrophage-based microrobots, we labeled the prepared 3D tumor spheroids with indocyanine green (ICG) to make them visible under OA imaging (Figure S17, Supporting Information). The macrophage-based microrobots were actuated by gradient pulling to the target tumor spheroid area, where their motion was monitored in real time using OA imaging (Figure 6C; Video S4, Supporting Information). In future work, macrophage-based microrobots may be distinguished from tumor spheroids by using a multiwavelength excitation design that uses more than one wavelength to image different chromophores. The background subtraction method could also be performed using advanced computational techniques.

We further investigated the antitumor activity of macrophage-based microrobots with a conditioned medium approach, in which the medium containing secreted molecules by one group of cells is harvested and transferred to another group of cells for further analysis.[6,69,70] After incubating the conditioned medium of macrophage-based microrobots with 3D tumor spheroids for 24 h, we investigated the viabilities of 3D tumor spheroids depending on two methodologies: membrane integrity measurements and metabolic activity measurements. Our membrane integrity measurements indicated that the incubation of 3D tumor spheroids with the medium of macrophage-based microrobots resulted mainly in dead cells after 24 h of incubation (Figure 6D). As an alternative method, we measured the viability of 3D tumor spheroids treated with the medium of macrophage-based microrobots by measuring intracellular ATP using CellTiter-Glo 3D Cell Viability assay. In contrast to live/dead staining, CellTiter-Glo 3D assay reagent can penetrate large spheroids, has an enhanced lytic capability, and, therefore, allows more sensitive and accurate viability determinations of 3D spheroids. As a result of the metabolic activity measurements, macrophage-based microrobots significantly suppressed the

© 2024 The Author(s). Advanced Healthcare Materials published by Wiley-VCH GmbH

21922659, 2024, 23, Downloaded from https://onlinelibrary.wiley.com/doi/10.1002/adhm.202400711 by Koc University, Wiley Online Library on [27/12/2024]. See the Terms and Conditions (https://onlinelibrary.wiley.com/terms-and-conditions) on Wiley Online Library for rules of use; OA articles are governed by the applicable Creative Commons License

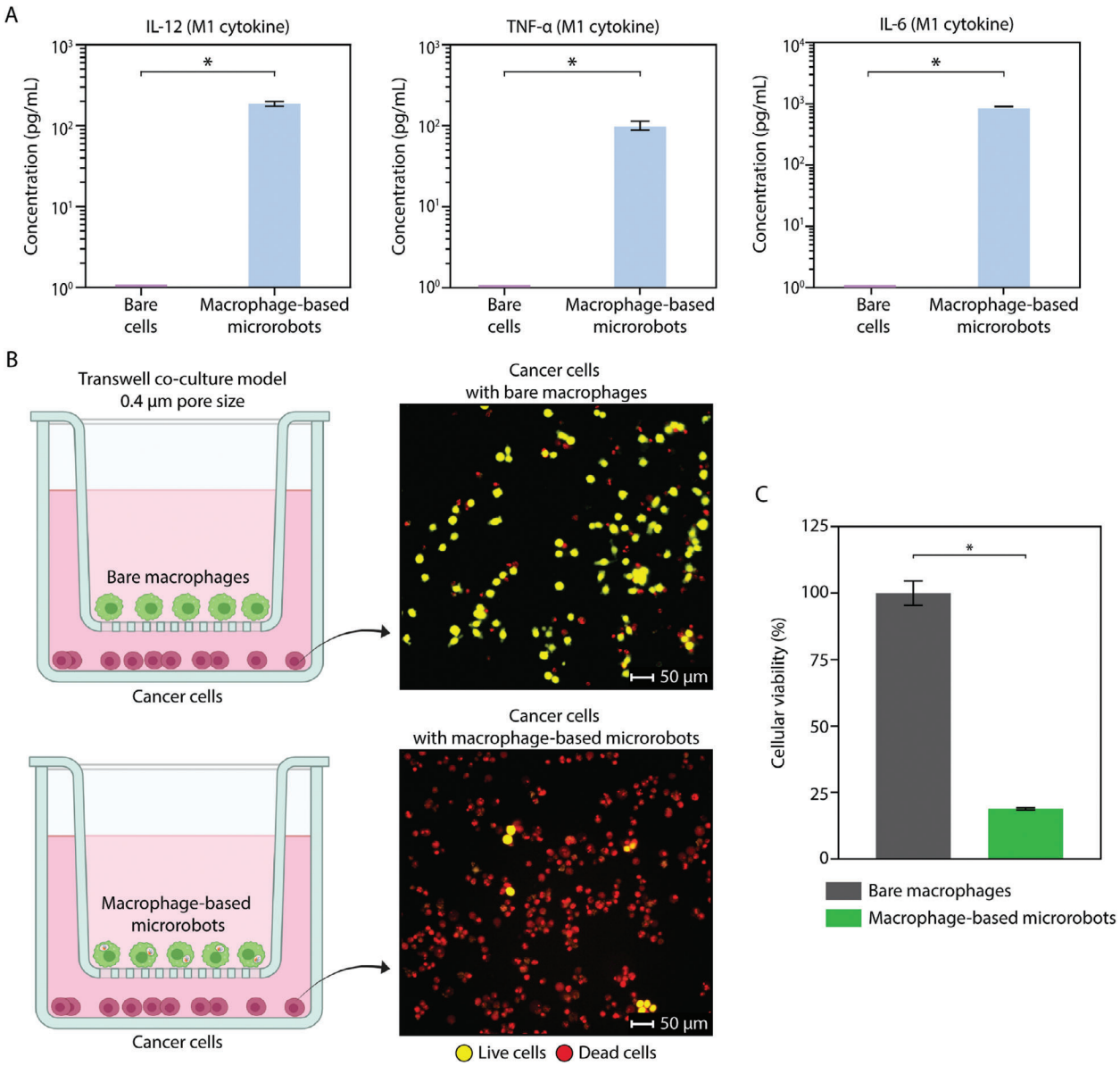


Figure 5. Antitumorigenic activities of macrophage-based microrobots. A) The M1 activation states of macrophage-based microrobots were characterized by measuring M1 cytokines (IL-12, TNF-α, and IL-6). The macrophage-based microrobots secreted significantly higher amounts of M1 cytokines than bare macrophages. Data were presented as mean ± SD, $n = 3$ (*, Student's t-test, $p < 0.05$). B) The antitumorigenic activities of macrophage-based microrobots were analyzed with co-culture experiments. The co-culture experiments were performed with a transwell insert with 0.4 μm pore sizes, where the urinary bladder cancer cells were co-cultured with bare macrophages or macrophage-based microrobots for 24 h. Representative live/dead fluorescence images of the cancer cells were acquired at 24 h of co-culture. Co-culturing cancer cells with macrophage-based microrobots resulted mainly in dead cells, whereas co-culturing cancer cells with bare macrophages led to most cancer cells remaining alive. C) Viability of cancer cells co-cultured with bare macrophages or macrophage-based microrobots for 24 h. Co-culturing macrophage-based microrobots with cancer cells reduced their viability to 19% at 24 h incubation. Data were presented as mean ± SD, $n = 3$ (*, Student's t-test, $p < 0.05$).

growth of 3D tumor spheroids, with viability of 0.8% after 24 h of incubation (Figure 6E).

3. Conclusion

Here, we presented macrophage-based microrobots developed from live macrophages and magnetic Janus particles. The magnetic Janus particles had two sides: the first side was FePt nanofilm for magnetic actuation, imaging, and tracking; and the second side was bacterial LPS for stimulating macrophages to a cancer-killing state. The incubation of magnetic Janus particles with macrophages enabled the remote magnetic control of macrophages, monitoring of macrophages under different imaging techniques (i.e., MRI and OA imaging), and suppressing the growth of monolayer and 3D tumor spheroids.

In this study, we indicated a biohybrid immune cell-based strategy, living macrophage-based microrobots, where remote magnetic actuation, antitumor abilities, and medical imaging

© 2024 The Author(s). Advanced Healthcare Materials published by Wiley-VCH GmbH

21922659, 2024, 23, Downloaded from https://onlinelibrary.wiley.com/doi/10.1002/adhm.202400711 by Koc University, Wiley Online Library on [27/12/2024]. See the Terms and Conditions (https://onlinelibrary.wiley.com/terms-and-conditions) on Wiley Online Library for rules of use; OA articles are governed by the applicable Creative Commons License

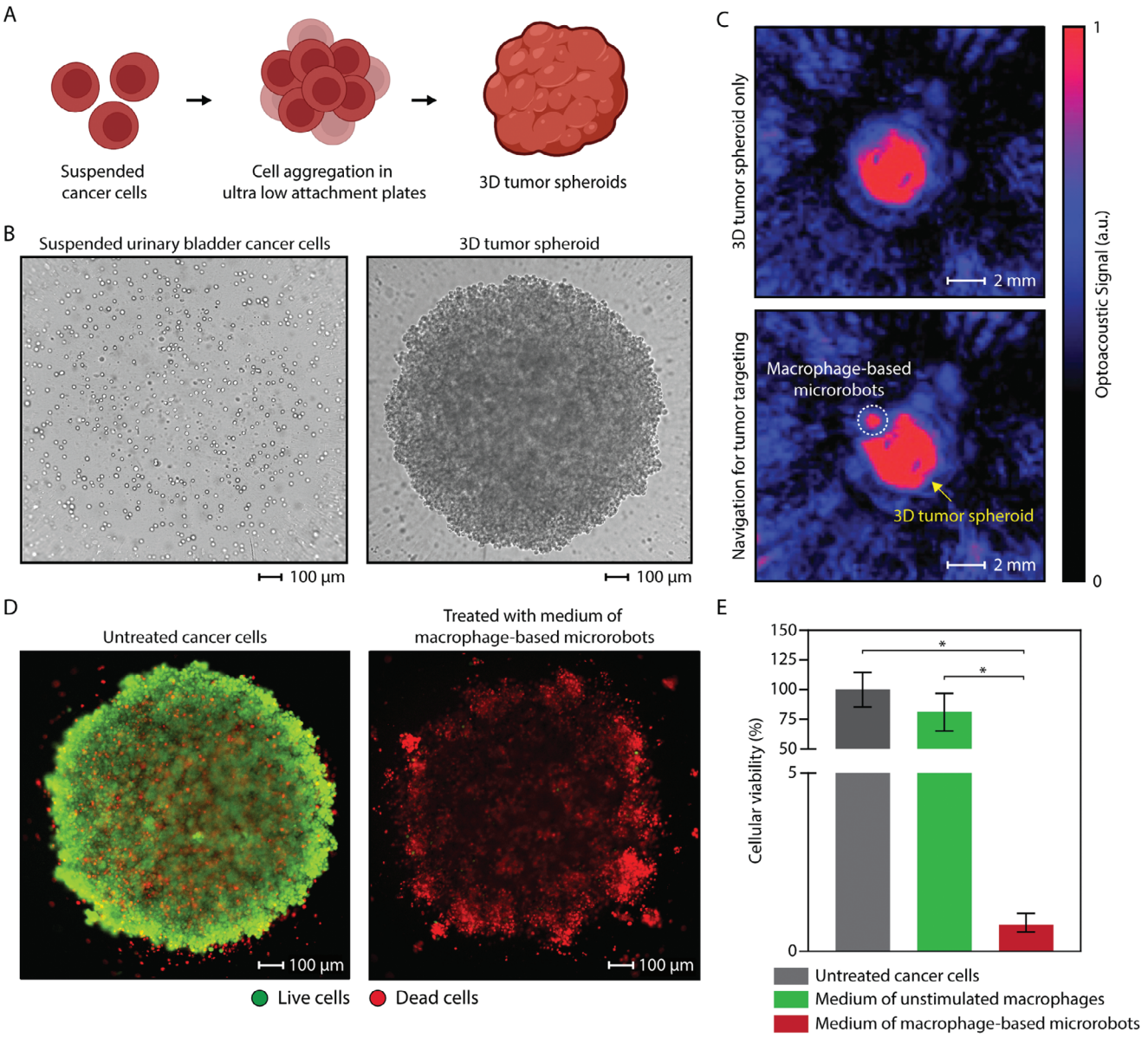


Figure 6. Macrophage-based microrobots for targeted tumor localization and treatment of urinary bladder 3D tumor spheroids. A) A schematic illustrates the preparation of 3D tumor spheroids. B) Bright-field microscopy images of suspended urinary bladder cancer cells and 3D tumor spheroid after incubation for 24 h. C) OA images of ICG-labeled single 3D tumor spheroid. Next, macrophage-based microrobots are magnetically navigated to the 3D tumor spheroid area using real-time OA imaging. D) Representative live/dead fluorescence images of 3D tumor spheroids after 24 h incubation with the fresh or conditioned medium of macrophage-based microrobots. Incubation of 3D tumor spheroids with the medium of macrophage-based microrobots resulted mainly in dead cells after 24 h of incubation. E) Viability of 3D tumor spheroids treated with the fresh medium as a control, conditioned medium of unstimulated macrophages, and conditioned medium of macrophage-based microrobots. The growth of 3D tumor spheroids was significantly suppressed by macrophage-based microrobots, with a viability of 0.8% after 24 h of incubation. Data were presented as mean ± SD, $n = 4$ (*, Student's t-test, $p < 0.05$).

are all combined in a single microrobotic design, all crucial for bringing medical microrobots into the clinics. Here, we indicated the suppression of urinary bladder cancer cells. Nonetheless, macrophage-based microrobots can potentially treat other cancer types (such as ovarian, breast, and lung), especially in vivo conditions, by sustaining inflammatory responses, secreting proinflammatory cytokines, and recruiting host immune cells to the disease site.[43,71] Our biohybrid microrobot design can help to improve the tumor-targeting and antitumor capabilities of macrophages by magnetically actuating and accumulating a swarm of macrophage-based microrobots at target locations, resulting in enhanced anticancer ability with minimal toxicity to the body. Furthermore, this biohybrid microrobot strategy can be developed to activate macrophages into anti-inflammatory (M2) states by altering the bacterial LPS layer with M2 stimuli for other medical applications, such as wound healing. Thus,

© 2024 The Author(s). Advanced Healthcare Materials published by Wiley-VCH GmbH

21922659, 2024, 23, Downloaded from https://onlinelibrary.wiley.com/doi/10.1002/adhm.202400711 by Koc University, Wiley Online Library on [27/12/2024]. See the Terms and Conditions (https://onlinelibrary.wiley.com/terms-and-conditions) on Wiley Online Library for rules of use; OA articles are governed by the applicable Creative Commons License

macrophage-based microrobots can be essential in future in vivo applications for treating diseases in hard-to-reach areas. In addition, since macrophages are derived from our own bodies, the developed macrophage-based microrobots can shape the future of personalized medicine by providing safe and effective immune cell-based therapies.

4. Experimental Section

Fabrication of Magnetic Janus Particles: Magnetic Janus particles were developed from 500 nm diameter silica particles (microParticles GmbH) coated with FePt magnetic film and bacterial LPS. For FePt magnetic film deposition, the silica particles were first uniformly distributed on an oxygen plasma-treated silicon wafer. The 60 nm thick FePt magnetic nanofilm was half-coated on silica particles using a molecular beam epitaxy chamber at ultrahigh vacuum conditions ($\approx(2–5) \times 10^{-9}$ mbar) with an annealing step at 680 °C for 1 h, as described and characterized previously.[37] After the FePt magnetic film deposition, the silica particles were detached from the silicon wafer by ultrasonication for further chemical processes.

Bacterial LPS was attached to the uncoated sides of the FePt-coated silica particles through bioconjugation (Figure S3A, Supporting Information).[73] The first step of the procedure was to attach amine groups (—NH_2) to the hydroxyl groups (—OH) of the FePt-coated Janus silica particles using 3-aminopropyltriethoxysilane (APTES, Sigma–Aldrich). The FePt-coated silica particles were vortexed in 1 mL ethanol solution with 50 µL APTES for 3 h, followed by incubation at 65 °C for 1 h. The particles were washed several times with ethanol and dimethyl sulfoxide (DMSO, Sigma–Aldrich). The second step of the procedure was to replace the amino groups with *N*-hydroxysuccinimide (NHS)–biotin. The particles were vortexed in 5 mg mL^{-1} EZ-link NHS–biotin (Thermo Fisher Scientific) in DMSO for 3 h, then washed multiple times with DMSO and Dulbecco's phosphate-buffered saline (DPBS, Gibco). The third step involved the conjugation of FITC-labeled streptavidin to the biotinylated ends of the particles. The particles vortexed with 50 µg mL^{-1} streptavidin solution in DPBS for 1 h, then washed multiple times with DPBS. As a final step, biotinylated LPS from *Escherichia coli* serotype 0111:B4 (InvivoGen) was conjugated to the particles via biotin–streptavidin interaction. The particles were vortexed with 500 µg mL^{-1} biotinylated bacterial LPS in DPBS for 1 h, then washed multiple times with DPBS. The resultant magnetic Janus particles, half-coated with magnetic FePt nanofilm and half-coated with bacterial LPS, were resuspended in DPBS and sterilized beneath ultraviolet light before further use.

Cell Culture: J774A.1 mouse peritoneal macrophages (American Type Culture Collection, ATCC) were cultured in sterile 75 cm^2 polystyrene cell culture flasks at 37 °C and 5% CO_2 atmosphere in high-glucose Dulbecco's modified Eagle's medium (DMEM, Gibco) supplemented with 10% fetal bovine serum (FBS, Gibco) and 1% penicillin/streptomycin (Gibco). At 80% confluence, the cells were detached from the surface using a cell scraper.

NUC-1 mouse urinary bladder cancer cells (Deutsche Sammlung von Mikroorganismen und Zellkulturen, DSMZ) were cultured in sterile 75 cm^2 polystyrene cell culture flasks at 37 °C and 5% CO_2 atmosphere in 45% Ham's F10 nutrient mix (Gibco), 45% DMEM (Gibco) supplemented with 10% FBS (Gibco), 1% penicillin/streptomycin (Gibco), 5 µg mL^{-1} human insulin (Sigma–Aldrich), 5 µg mL^{-1} human transferrin (Sigma–Aldrich), 50 nM hydrocortisone (Sigma–Aldrich), and 5 ng mL^{-1} selenite (Sigma–Aldrich). At 80% confluence, the cells were detached from the surface using 0.25% (w/v) trypsin/ethylenediaminetetraacetic acid (EDTA) solution.

HT-29 human colorectal adenocarcinoma cells (ATCC) were cultured in sterile 75 cm^2 polystyrene cell culture flasks at 37 °C and 5% CO_2 atmosphere in high-glucose DMEM (Gibco) supplemented with 10% FBS (Gibco) and 1% penicillin/streptomycin (Gibco). At 80% confluence, the cells were detached from the surface using 0.25% (w/v) trypsin/EDTA solution.

Preparation of Macrophage-Based Microrobots: J774A.1 mouse peritoneal macrophage cells were first seeded on a 6-well plate at a concentration of 3×10^5 cells in a 2 mL medium 1 day before the experiment. After overnight incubation, magnetic Janus particles were diluted in the cell culture medium of J774A.1 cells at a concentration of 0.05 mg mL^{-1}. The J774A.1 cells were incubated overnight with a medium containing magnetic Janus particles. Ultimately, the J774A.1 cells phagocytosed the magnetic Janus particles, where the resultant cells were called macrophage-based microrobots.

Confocal Imaging: Macrophage-based microrobots were fixed in 4% (v/v) paraformaldehyde (PFA, Alfa Aesar) in DPBS for 20 min. The cells were then permeabilized with 0.1% (v/v) Triton-X-100 (Sigma–Aldrich) in DPBS for 15 min. For staining, DPBS solution containing 1 µg mL^{-1} Hoechst 33342 (Thermo Fisher Scientific) and 2 drops mL^{-1} ActinRed 555 ReadyProbes (Life Technologies) was applied to cells for 30 min in the dark. The confocal images of macrophage-based microrobots were acquired using Leica SP8 confocal microscopy.

Imaging of Macrophage-Based Microrobots in Soft-Tissue-Mimicking Phantoms: Bare macrophages and macrophage-based microrobots were dispersed and immobilized in 1% (w/v) ultralow gelling temperature agarose (Sigma–Aldrich) in 96-well plates at various concentrations (500 000, 250 000, 100 000, 50 000, 10 000, and 1000 cells in 100 µL solution). The prepared samples were imaged using both MRI and OA imaging. OA imaging was performed with a handheld, 3D optoacoustic transducer (MSOT inVision 512-Echo, iThera Medical), where OA signals were collected at different wavelengths for all groups. The optimum wavelength for macrophage-based microrobots was 840 nm.

MRI experiments were conducted using a 7 Tesla Biospec Bruker system with an actively shielded gradient system (BGA20SHP) and a 40 mm diameter quadrature birdcage coil. Different concentrations of bare macrophages and macrophage-based microrobots were imaged using a 3D gradient echo imaging sequence (repetition time (TR) = 100 ms, echo time (TE) = 6 ms, $100 \times 100 \times 100$ μm^3 in-plane resolution, number of excitations (NEX) = 8, total scan duration 2.7 h).

Ex Vivo Imaging of Macrophage-Based Microrobots: The BALB/c mice were freshly euthanized at the Institute of Comparative Molecular Endocrinology, Center for Biomedical Research, University of Ulm according to §4 (3) TierSchG (animal welfare/protection law) (official permission number: MPIISS-UUL-o.189-31), and immediately used for further experiments.

For ex vivo MRI experiments, bare macrophages and macrophage-based microrobots were dissolved in DPBS at different concentrations (250 000, 166 667, and 1667 cells in a 20 µL injection volume) and injected into the left and right back muscles of dead BALB/c mice. A 2D gradient echo imaging sequence (TR/TE 500/7 ms, 100×100 μm^2 in-plane resolution, slice thickness 0.5 mm, NEX = 4, total scan duration 10 min) was used to image mice ($N = 4$) before and immediately after the injection of macrophage-based microrobots.

For ex vivo OA imaging experiments, the macrophage-based microrobot was injected into the back muscle of the dead animal at a concentration of 1500 000 cells in a 50 µL injection volume using a 30 G needle. The animal was scanned with a handheld, 3D optoacoustic transducer (MSOT inVision 512-Echo, iThera Medical) before and after the injection of microrobots, and the signals were collected at different wavelengths.

Optoacoustic Imaging-Guided Magnetic Actuation of Macrophage-Based Microrobots: The macrophage-based microrobots were dispersed in DPBS and placed in tubing for real-time imaging of macrophage-based microbots in static conditions using an MSOT inVision 512-echo OA system (iThera Medical). The macrophage-based microrobots were magnetically actuated with an average velocity of 1 mm s^{-1} using a permanent magnet and imaged in real time using the 3D optoacoustic transducer (iThera Medical).

Flow experiments were conducted in a tubing (Cole-Parmer) with an inner and an outer diameter of 0.25 and 0.76 mm, respectively. The flow rates of microrobots were controlled using a syringe pump (KD Scientific Inc.). The volume flow rates of 4 µL min^{-1} in the syringe pump resulted in an average flow rate of 1.3 mm s^{-1}. The macrophage-based microrobots were collected at the targeted location using a permanent magnet under

© 2024 The Author(s). Advanced Healthcare Materials published by Wiley-VCH GmbH

21922659, 2024, 23, Downloaded from https://onlinelibrary.wiley.com/doi/10.1002/adhm.202400711 by Koc University, Wiley Online Library on [27/12/2024]. See the Terms and Conditions (https://onlinelibrary.wiley.com/terms-and-conditions) on Wiley Online Library for rules of use; OA articles are governed by the applicable Creative Commons License

flow conditions. The real-time videos were recorded with an OA device (MSOT inVision 512-Echo, iThera Medical).

FEM Simulations: For FEM simulations, commercial FEM software (COMSOL Multiphysics 5.6, COMSOL Inc.) was used. Simulations were implemented to estimate flow velocity magnitudes, and they were 3D based on Navier–Stokes equations. The inner diameter of the fluid channel was 0.25 µmm. The average velocity of the deionized water was 1.3 mm s^{-1}. Boundary conditions of the walls were assigned as no-slip conditions.

M1 Characterization: Activation states of macrophage-based microrobots were characterized by measuring the expressions of M1 cytokines (IL-12, TNF-α, and IL-6). J774A.1 cells were seeded on a 24-well plate at 3×10^5 cells per well in triplicates. After overnight incubation, the cells were i) untreated or ii) treated with magnetic Janus particles for 24 h. The supernatant from all groups was collected, and secreted cytokines were analyzed using IL-12, TNF-α, and IL-6 enzyme-linked immunosorbent assay (ELISA) sets (BD Biosciences) following the supplier's instructions. The optical densities were measured using a microplate reader (Tecan, Infinite M Plex).

Co-Culture Experiments: 6.5 mm diameter inserts, 0.4 µm pore size, tissue culture treated, polycarbonate membrane, and sterile polystyrene plates (Corning) were used for co-culture experiments. A day before, macrophages were seeded at 2.5×10^4 cells per well in their natural growth medium on the transwell insert (upper chamber). After overnight incubation, the macrophages were untreated or treated with 0.05 mg mL^{-1} magnetic Janus particles, whereas the NUC-1 urinary bladder cancer cells were seeded to the bottom chamber at a concentration of 5×10^4 cells per well. At 24 h of co-culture, the cell viabilities of NUC-1 cells were measured using Live/Dead Cell Imaging Kit (Invitrogen) and CellTiter-Glo Cell Viability Assay (Promega) according to the manufacturer's instructions.

Preparation of 3D Tumor Spheroids: HT-29 tumor spheroids were used for OA imaging experiments. HT-29 cells were seeded in Nunclon Sphera-treated, U-shaped-bottomed 96-well plates (Thermo Fisher Scientific) at 5×10^4 cells per well and incubated at 37 °C and 5% CO_2 atmosphere as previously described.[72] On day 3, HT-29 tumor spheroids were almost 1 mm in diameter. To make the 3D tumor spheroids visible under OA imaging, HT-29 spheroids were labeled with ICG (0.1 mg mL^{-1}) overnight. The ICG-labeled 3D tumor spheroids were washed multiple times with DPBS and used for further experiments. The HT-29 colon cancer 3D tumor spheroids and macrophage-based microrobots were placed in a 6 cm Petri dish for OA imaging. A permanent magnet was used to actuate and steer around 1×10^6 macrophage-based microrobots toward the HT-29 3D tumor spheroids. A 3D handheld optoacoustic probe (MSOT inVision 512-Echo, iThera Medical) was used to capture the videos.

Assessment of 3D Tumor Spheroids Death: Antitumor activities of macrophage-based microrobots were performed with NUC-1 tumor spheroids. NUC-1 cells were seeded in Nunclon Sphera-treated, U-shaped-bottomed 96-well plates in triplicates (Thermo Fisher Scientific) at 1×10^4 cells per well and incubated at 37 °C and 5% CO_2 atmosphere. The NUC-1 spheroids were treated with i) their natural growth medium, ii) medium harvested from macrophages treated with LPS-free FePt-coated silica particles (50% fresh NUC-1 medium, and 50% conditioned medium of unstimulated macrophages), or iii) medium harvested from macrophage-based microrobots (50% fresh NUC-1 medium and 50% conditioned medium of macrophage-based microrobots) for 24 h. After 24 h of incubation, the NUC-1 cells were stained with a Live/Dead Cell Imaging Kit (Invitrogen) according to the manufacturer's instructions.

CellTiter-Glo 3D Cell Viability Assay (Promega) was also used to measure ATP levels in NUC-1 cells. Briefly, an equal volume of CellTiter-Glo 3D reagent was added to the cells, mixed for 5 min for cell lysis, and the signal was stabilized for 25 min at room temperature. Luminescence values were then measured with a microplate reader (Tecan, Infinite M Plex) in a 96-well black/clear bottom plate (Thermo Fisher Scientific).

Statistical Analysis: The measurements were conducted in at least three replicates for each group. The numerical values were presented as means ± standard deviation (SD) of the means. Statistical analysis was performed using Student's *t*-test, and a *p*-value of less than 0.05 was considered significant.

Supporting Information

Supporting Information is available from the Wiley Online Library or from the author.

Acknowledgements

This study was funded by the Max Planck Society. The schematics of the paper were created with BioRender.com. The authors thank Devin Sheehan for the flow cytometry analysis and Anitha Shiva for helping with SEM imaging and VSM measurements.

Open access funding enabled and organized by Projekt DEAL.

Conflict of Interest

The authors declare no conflict of interest.

Data Availability Statement

The data that support the findings of this study are available from the corresponding author upon reasonable request.

Keywords

biohybrid microrobots, cancer immunotherapy, cell-based microrobots, cell tracking, immunobots, medical imaging, medical microrobots

Received: February 23, 2024
Revised: May 17, 2024
Published online: June 25, 2024

[1] H. Ceylan, J. Giltinan, K. Kozielski, M. Sitti, *Lab Chip.* **2017**, *17*, 1705.
[2] B. J. Nelson, I. K. Kaliakatsos, J. J. Abbott, *Annu. Rev. Biomed. Eng.* **2010**, *12*, 55.
[3] M. Sitti, *Mobile Microrobotics*, MIT Press, Cambridge, MA, **2017**.
[4] M. Sitti, H. Ceylan, W. Hu, J. Giltinan, M. Turan, S. Yim, E. Diller, *Proc. IEEE.* **2015**, *103*, 205.
[5] H. Ceylan, N. O. Dogan, I. C. Yasa, M. N. Musaoglu, Z. U. Kulali, M. Sitti, *Sci. Adv.* **2021**, *7*, eabh0273.
[6] N. O. Dogan, H. Ceylan, E. Suadiye, D. Sheehan, A. Aydin, I. C. Yasa, A. M. Wild, G. Richter, M. Sitti, *Small.* **2022**, *18*, 2204016.
[7] K. T. Roybal, W. A. Lim, *Annu. Rev. Immunol.* **2017**, *35*, 229.
[8] W. Zeng, P. Zhang, *Exp. Cell Res.* **2022**, *410*, 112971.
[9] L. M. Bush, C. P. Healy, S. B. Javdan, J. C. Emmons, T. L. Deans, *Trends Pharmacol. Sci.* **2021**, *42*, 106.
[10] N. Kapate, R. Liao, R. L. Sodemann, T. Stinson, S. Prakash, N. Kumbhojkar, V. C. Suja, L. L.-W. Wang, M. Flanz, R. Rajeev, *PNAS Nexus.* **2024**, *3*, pgad434.
[11] C. W. Shields iv, M. A. Evans, L. L.-W. Wang, N. Baugh, S. Iyer, D. Wu, Z. Zhao, A. Pusuluri, A. Ukidve, D. C. Pan, S. Mitragotri, *Sci. Adv.* **2020**, *6*, eaaz6579.
[12] D. J. Irvine, M. V. Maus, D. J. Mooney, W. W. Wong, *Science* **2022**, *378*, 853.
[13] N. Kumbhojkar, S. Prakash, T. Fukuta, K. Adu-Berchie, N. Kapate, R. An, S. Darko, V. C. Suja, K. S. Park, A. P. Gottlieb, M. G. Bibbey, M. Mukherji, L. L.-W. Wang, D. J. Mooney, S. Mitragotri, *Nat. Biomed. Eng.* **2024**, *8*, 579.
[14] A. E.-H. El-Kadiry, M. Rafei, R. Shammaa, *Front. Med.* **2021**, *8*, 756029.

© 2024 The Author(s). Advanced Healthcare Materials published by Wiley-VCH GmbH

21922659, 2024, 23, Downloaded from https://onlinelibrary.wiley.com/doi/10.1002/adhm.202400711 by Koc University, Wiley Online Library on [27/12/2024]. See the Terms and Conditions (https://onlinelibrary.wiley.com/terms-and-conditions) on Wiley Online Library for rules of use; OA articles are governed by the applicable Creative Commons License

[15] I. C. Yasa, H. Ceylan, U. Bozuyuk, A.-M. Wild, M. Sitti, *Sci. Rob.* **2020**, *5*, eaaz3867.
[16] J. Han, J. Zhen, V. Du Nguyen, G. Go, Y. Choi, S. Y. Ko, J.-O. Park, S. Park, *Sci. Rep.* **2016**, *6*, 28717.
[17] V. D. Nguyen, H.-K. Min, H. Y. Kim, J. Han, Y. H. Choi, C.-S. Kim, J.-O. Park, E. Choi, *ACS Nano.* **2021**, *15*, 8492.
[18] V. D. Nguyen, J.-O. Park, E. Choi, *Biomimetics.* **2023**, *8*, 553.
[19] L. P. Jahromi, M. A. Shahbazi, A. Maleki, A. Azadi, H. A. Santos, *Adv. Sci.* **2021**, *8*, 2002499.
[20] T. A. Butterfield, T. M. Best, M. A. Merrick, *J. Athl. Train.* **2006**, *41*, 457.
[21] S. Epelman, K. J. Lavine, G. J. Randolph, *Immunity.* **2014**, *41*, 21.
[22] D. Hirayama, T. Iida, H. Nakase, *Int. J. Mol. Sci.* **2017**, *19*, 92.
[23] N. R. Anderson, N. G. Minutolo, S. Gill, M. Klichinsky, *Cancer Res.* **2021**, *81*, 1201.
[24] E. Cendrowicz, Z. Sas, E. Bremer, T. P. Rygiel, *Cancers.* **2021**, *13*, 1946.
[25] Y. Pan, Y. Yu, X. Wang, T. Zhang, *Front. Immunol.* **2020**, *11*, 583084.
[26] M. Reis-Sobreiro, A. Teixeira da Mota, C. Jardim, K. Serre, *Cells* **2021**, *10*, 2364.
[27] N. Kumari, S. H. Choi, *J. Exp. Clin. Cancer Res.* **2022**, *41*, 68.
[28] Z. Duan, Y. Luo, *Signal Transduct. Target Ther.* **2021**, *6*, 127.
[29] J. J. Connell, P. S. Patrick, Y. Yu, M. F. Lythgoe, T. L. Kalber, *Regener. Med.* **2015**, *10*, 757.
[30] M. Muthana, A. J. Kennerley, R. Hughes, E. Fagnano, J. Richardson, M. Paul, C. Murdoch, F. Wright, C. Payne, M. F. Lythgoe, *Nat. Commun.* **2015**, *6*, 8009.
[31] A. Aziz, S. Pane, V. Iacovacci, N. Koukourakis, J. Czarske, A. Menciassi, M. Medina-Sánchez, O. G. Schmidt, *ACS Nano.* **2020**, *14*, 10865.
[32] S. James, K. Neuhaus, M. Murphy, M. Leahy, *Stem Cell Res. Ther.* **2021**, *12*, 511.
[33] C. Zhang, J. Zhang, J. Niu, Z. Zhou, J. Zhang, Z. Tian, *Hum. Immunol.* **2008**, *69*, 490.
[34] Q. Wang, J. Zhang, J. Yu, J. Lang, Z. Lyu, Y. Chen, L. Zhang, *ACS Nano.* **2023**, *17*, 13081.
[35] C. M. Oral, M. Pumera, *Nanoscale* **2023**, *15*, 8491.
[36] H. Zhang, Z. Li, C. Gao, X. Fan, Y. Pang, T. Li, Z. Wu, H. Xie, Q. He, *Sci. Rob.* **2021**, *6*, eaaz9519.
[37] U. Bozuyuk, E. Suadiye, A. Aghakhani, N. O. Dogan, J. Lazovic, M. E. Tiryaki, M. Schneider, A. C. Karacakol, S. O. Demir, G. Richter, *Adv. Funct. Mater.* **2022**, *32*, 2109741.
[38] D. Zhuang, H. Zhang, G. Hu, B. Guo, *J. Nanobiotechnol.* **2022**, *20*, 1.
[39] S.-W. Chou, Y.-H. Shau, P.-C. Wu, Y.-S. Yang, D.-B. Shieh, C.-C. Chen, *J. Am. Chem. Soc.* **2010**, *132*, 13270.
[40] H. Yang, J. Zhang, Q. Tian, H. Hu, Y. Fang, H. Wu, S. Yang, *J. Magn. Magn. Mater.* **2010**, *322*, 973.
[41] M. González, L. A. Bagatolli, I. Echabe, J. L. Arrondo, C. E. Argarana, C. R. Cantor, G. D. Fidelio, *J. Biol. Chem.* **1997**, *272*, 11288.
[42] N. B. Day, C. R. Orear, A. C. Velazquez-Albino, H. J. Good, A. Melnyk, C. M. Rinaldi-Ramos, C. W. Shields iv, *ACS Appl. Bio Mater.* **2023**.
[43] Y. Huo, H. Zhang, L. Sa, W. Zheng, Y. He, H. Lyu, M. Sun, L. Zhang, L. Shan, A. Yang, *J. Transl. Med.* **2023**, *21*, 225.
[44] A. Mantovani, P. Allavena, F. Marchesi, C. Garlanda, *Nat. Rev. Drug Discov.* **2022**, *21*, 799.
[45] X. Zhou, X. Liu, L. Huang, *Adv. Funct. Mater.* **2021**, *31*, 2006220.
[46] H. Ceylan, I. C. Yasa, U. Kilic, W. Hu, M. Sitti, *Prog. Biomed. Eng.* **2019**, *1*, 012002.
[47] S. Martel, O. Felfoul, J.-B. Mathieu, A. Chanu, S. Tamaz, M. Mohammadi, M. Mankiewicz, N. Tabatabaei, *Int. J. Robot. Res.* **2009**, *28*, 1169.
[48] M. E. Tiryaki, M. Sitti, *Adv. Intell. Syst.* **2022**, *4*, 2100178.
[49] P. Wrede, O. Degtyaruk, S. K. Kalva, X. L. Deán-Ben, U. Bozuyuk, A. Aghakhani, B. Akolpoglu, M. Sitti, D. Razansky, *Sci. Adv.* **2022**, *8*, eabm9132.
[50] X. Yan, Q. Zhou, M. Vincent, Y. Deng, J. Yu, J. Xu, T. Xu, T. Tang, L. Bian, Y.-X. J. Wang, *Sci. Rob.* **2017**, *2*, eaaq1155.
[51] G. A. Tural, U. Bozuyuk, N. O. Dogan, Y. Alapan, M. B. Akolpoglu, A. Aghakhani, J. Lazovic, O. Ozer, M. Sitti, *Adv. Ther.* **2024**, *7*, 2300319.
[52] V. Ntziachristos, D. Razansky, *Chem. Rev.* **2010**, *110*, 2783.
[53] A. Aziz, R. Nauber, A. S. Iglesias, M. Tang, L. Ma, L. M. Liz-Marzán, O. G. Schmidt, M. Medina-Sánchez, *J. Microbio. Robot.* **2023**, *19*, 37.
[54] D. Razansky, M. Distel, C. Vinegoni, R. Ma, N. Perrimon, R. W. Köster, V. Ntziachristos, *Nat. Photonics.* **2009**, *3*, 412.
[55] L. Xie, X. Pang, X. Yan, Q. Dai, H. Lin, J. Ye, Y. Cheng, Q. Zhao, X. Ma, X. Zhang, *ACS Nano.* **2020**, *14*, 2880.
[56] F. Galli, M. Varani, C. Lauri, G. G. Silveri, L. Onofrio, A. Signore, *EJNMMI Radiopharm. Chem.* **2021**, *6*, 7.
[57] L. Tong, H. Zhao, Z. He, Z. Li, in *Medical Imaging in Clinical Practice*, IntechOpen, London **2013**, p. 63.
[58] N. Mahkam, A. Aghakhani, D. Sheehan, G. Gardi, R. Katzschmann, M. Sitti, *Adv. Sci.* **2023**, *10*, 2304233.
[59] D. Son, M. C. Ugurlu, M. Sitti, *Sci. Adv.* **2021**, *7*, eabi8932.
[60] K. Manickam, R. R. Machireddy, S. Seshadri, *J. Mech. Behav. Biomed. Mater.* **2014**, *35*, 132.
[61] C. K. McGarry, L. J. Grattan, A. M. Ivory, F. Leek, G. P. Liney, Y. Liu, P. Miloro, R. Rai, A. P. Robinson, A. J. Shih, *Phys. Med. Biol.* **2020**, *65*, 23TR01.
[62] A. Tejo-Otero, F. Fenollosa-Artés, I. Achaerandio, S. Rey-Vinolas, I. Buj-Corral, M. Á. Mateos-Timoneda, E. Engel, *Gels.* **2022**, *8*, 40.
[63] K. Hasenbach, S. Wiehr, C. Herrmann, J. Mannheim, F. Cay, G. von Kürthy, T. Bolmont, S. A. Grathwohl, M. Weller, C. Lengerke, *Neurooncol.* **2012**, *14*, 471.
[64] D. Shen, G. Wu, H.-I. Suk, *Annu. Rev. Biomed. Eng.* **2017**, *19*, 221.
[65] D. Laha, R. Grant, P. Mishra, N. Nilubol, *Front. Immunol.* **2021**, *12*, 656908.
[66] S. T. Orange, J. Leslie, M. Ross, D. A. Mann, H. Wackerhage, *Trends Endocrinol. Metab.* **2023**, *34*, 749.
[67] Y. Chen, Y. Song, W. Du, L. Gong, H. Chang, Z. Zou, *J. Biomed. Sci.* **2019**, *26*, 1.
[68] J. Yoo, Y. Jung, K. Char, Y. Jang, *Trends Biotechnol.* **2023**, *41*, 214.
[69] N. O. Dogan, U. Bozuyuk, P. Erkoc, A. C. Karacakol, A. Cingoz, F. Seker-Polat, M. A. Nazeer, M. Sitti, T. Bagci-Onder, S. Kizilel, *Adv. Nanobiomed. Res.* **2022**, *2*, 2100033.
[70] A. Engström, A. Erlandsson, D. Delbro, J. Wijkander, *Int. J. Oncol.* **2014**, *44*, 385.
[71] A. Viola, F. Munari, R. Sánchez-Rodríguez, T. Scolaro, A. Castegna, *Front. Immunol.* **2019**, *10*, 1462.
[72] R. H. Soon, Z. Yin, M. A. Dogan, N. O. Dogan, M. E. Tiryaki, A. C. Karacakol, A. Aydin, P. Esmaeili-Dokht, M. Sitti, *Nat. Commun.* **2023**, *14*, 3320.
[73] M. Han, E. Yildiz, U. Bozuyuk, A. Aydin, Y. Yu, A. Bhargava, S. Karaz, M. Sitti, *Nat. Commun.* **2024**, *15* https://doi.org/10.1038/s41467-024-46245-4.

© 2024 The Author(s). Advanced Healthcare Materials published by Wiley-VCH GmbH

21922659, 2024, 23, Downloaded from https://onlinelibrary.wiley.com/doi/10.1002/adhm.202400711 by Koc University, Wiley Online Library on [27/12/2024]. See the Terms and Conditions (https://onlinelibrary.wiley.com/terms-and-conditions) on Wiley Online Library for rules of use; OA articles are governed by the applicable Creative Commons License